Looking for quantum effects in magnetic nanoparticles using the molecular nanomagnet approach

M. Fittipaldi,[1,*] C. Innocenti,[1] P. Ceci,[2] C. Sangregorio,[1,3,†] L. Castelli,[1] L. Sorace,[1] and D. Gatteschi[1]

[1]*INSTM and Department of Chemistry "U. Schiff," University of Florence, via della Lastruccia, 3-13 50019 Sesto Fiorentino, Italy*

[2]*CNR, Institute of Molecular Biology and Pathology, 00185 Rome, Italy*

[3]*CNR-ISTM Milano, via C. Golgi 19, 20133 Milano, Italy*

(Received 16 September 2010; revised manuscript received 14 October 2010; published 17 March 2011)

In an effort to build a unitary view of the properties of magnetic nanoparticles (MNPs) and molecular nanomagnets (MNMs), we investigated with different techniques MNPs of spinel-type iron oxide of approximately 3.5 and 8 nm mineralized in the internal cavity of ferritin-type proteins. In particular, we used electron magnetic resonance (EMR) and static and dynamic magnetic measurements and took advantage of the capacity of the protein shells to control the size of the MNPs. A signal at half-field in the EMR spectrum is observed for MNPs as big as 8 nm mineralized in protein cavities. This feature has been interpreted as the signature of the discrete structure of the energy levels and, therefore, of the quantum nature of the system. The EMR behavior of the MNPs is compared with that of two large MNMs: one containing 19 Fe(III) and a second containing 19 Mn(II) centers. The ideal structure of the latter is used as a model to show the structuring of the energy levels. In particular, the analysis of MNP behavior based on the MNM approach helps to shed light on the role of the different energy terms that govern the MNP properties.

DOI: 10.1103/PhysRevB.83.104409 PACS number(s): 75.75.Fk, 76.30.−v, 75.50.Tt, 75.30.Gw

I. INTRODUCTION

There is a great interest in the investigation of nanomagnetic systems prompted both by the high technological impact[1] of these systems (catalysis,[2] data storage,[3] spintronics,[4] MRI,[5,6] magnetic fluids,[7] biotechnology and biomedicine,[8,9] and environmental remediation[10,11]) and their relevance for fundamental science.[12,13] Two classes of zero-dimensional objects may be distinguished within the nanomagnetic world: magnetic nanoparticles (MNPs) and molecular nanomagnets (MNMs). Up to now, two distinct approaches have been followed for their preparation and the rationalization of their properties. The synthesis and description of MNMs is characterized by a bottom-up approach, which searches for the emergence of bulk properties starting from those of the single ions. On the other hand, MNPs are characterized by a top-down approach, which searches for the change in the properties of the bulk material induced by the size reduction.[12] Theoretically, MNMs are described by quantum mechanics starting from the single ion, while MNPs are generally described by classical mechanics. The two classes of systems are approaching similar size with a comparable number of metal ions, of the order of 10^2, which poses the need for a unified description.[12] The molecular basis of MNMs ensures that we are dealing with an ensemble of identical objects. This is more difficult to achieve in MNPs. This has hampered and delayed a fine characterization of MNP properties at the level reached in MNMs. The significant improvement in recent years in the synthesis of MNPs[3,5,14] has determined narrower size distributions of the samples, which can result in a better correlation between the physical properties and the structural data, as well as in the understanding of the role of defective structures.

Electron magnetic resonance (EMR) has been a fundamental tool in the understanding of MNM properties.[15–19] The spin Hamiltonian formalism has been widely used and allowed detailed correlation between the obtained parameters and structural data, and the low-temperature spin dynamics of these systems. In this respect, particular attention has been devoted to the use of EMR for the accurate determination of the magnetic anisotropy responsible for the energy barrier to be overcome to reverse the magnetic moment, which is the key feature of the peculiar magnetic behavior of both MNMs and MNPs.

EMR is thus expected to have great importance also in understanding the properties of MNPs,[12] as will be apparent from the work presented here. Up to now, this technique has not been a standard tool for the characterization of MNP properties. The EMR spectra of MNPs have generally been interpreted in a classical framework, in which, however, the temperature behavior of the EMR spectra is not reproduced.[20,21] Moreover, the appearance of quantum effects,[22–24] signature of a discrete structure of the energy levels, cannot be predicted. Recently, a different approach has been proposed in which 5 nm MNPs have been treated as a giant spin with quantum nature.[25] This has stimulated a different and interesting view on the subject; however, open questions still remain as well as the need to justify some assumptions of the model.

To get a deeper understanding of the properties of MNPs, we have performed a magnetic and EMR characterization of maghemite/magnetite MNPs of different sizes. The MNPs have been mineralized inside the internal cavity of two different protein cages, namely the Dps protein from *Listeria innocua* (LiDps)[26] and the ferritin protein from the hyperthermophilic archaeon *Pyrococcus furiosus* (PfFt).[27] Protein cages can be viewed as nanoreactors which allow chemical reactions to take place in a confined environment shielded from bulk solution.[22,28] In particular, the use of LiDps and PfFt resulted in the efficient synthesis of MNPs characterized by a narrow size distribution (3.4 ± 1.0 and 7.7 ± 1.4 nm, respectively).

To push forward the information that can be obtained by EMR spectroscopy, the orientation dependence of the spectra of a suspension of MNPs, frozen in the presence of an

external magnetic field, was analyzed. This method allows us to obtain more direct information similarly to what occurs in single-crystal EMR studies. This procedure has already been exemplarily employed by Li *et al.*[29] to determine the energy barriers of MNPs grown in Dps, virus, and ferritin cages. We followed the same experimental approach, but we collected the EMR spectra at different temperatures, thus enabling the observation of more structures. This approach allowed us to focus on a subensemble of MNPs with more homogeneous magnetic properties that can be more easily compared with those of MNMs. The results obtained are then compared with those of a high spin Fe-based MNM (Fe_{19}),[30] which some of us have recently studied by single-crystal EMR.[31] The structure of the Fe_{19} cluster shows a strong similarity with that of a Mn_{19} cluster,[32] which has an almost ideal brucite growth mode and will be used as a model to show the structuring of the energy levels. The overall comparison of MNMs and MNPs gives new insight into the MNP properties.

II. EXPERIMENTAL

A. MNP synthesis in LiDps and PfFt proteins

Apo-LiDps and apo-PfFt proteins were expressed and purified as reported elsewhere.[22,27] Iron incorporation experiments were carried out at 65 °C on 1 mg/mL LiDps or PfFt samples in 5 mM Hepes-NaOH at a pH of 8.5. Solutions of $FeSO_4$ dissolved in 0.5 mM HCl were used as an iron source. During the course of the experiment, the reaction vessel was kept at 65 °C under a positive N_2 pressure, and the pH was maintained dynamically at 8.5 with 100 mM NaOH by means of an automatic titrator (TITRINO, Metrohm AG). Solutions of $FeSO_4$ (15 mM) and H_2O_2 (5 mM) were added simultaneously and at a constant rate (0.5 mL/min) using two peristaltic pumps. The iron loading factor was 450 or 4500 Fe(II)/protein. Any aggregate of protein and iron oxides produced during MNP formation were removed by centrifugation at 16000 rpm for 45 min at 4 °C and by filtration through 0.2-μm filters. MNPs were purified by size exclusion chromatography (SEC) using a Superose 6 gel-filtration column equilibrated with 0.15 M HEPES-NaOH buffer at pH 7.8. The protein and iron contents in the samples containing MNPs were assessed by means of native electrophoresis on 1% agarose gels and of the ferrozine method as described in Ceci *et al.*[22]

B. Morphological and physical characterization

Sedimentation velocity studies were carried out to assess the molecular mass and size distribution of the protein-enclosed MNP samples. The experiments were conducted as described in Kasyutich *et al.*[27] The fitting procedures yielded a root mean square deviation (rmsd) of 0.005. The particle size distributions were calculated by converting the $c(s)$ distributions in $c(d)$ (size distributions) and taking into account the densities of bulk maghemite and protein shell and the thickness of the protein shell.

Particle diameter and size distribution of the inorganic cores were also determined by transmission electron microscopy (TEM) images obtained by a CM12 PHILIPS microscope. Samples were prepared by drop-drying a diluted suspension of nanoparticles onto 200 mesh carbon-coated copper grids. The recorded images were analyzed by the software Image Pro-Plus©, and the mean diameter and the size distribution were obtained from a statistic over ∼700 nanoparticles. X-ray diffraction (XRD) patterns were recorded on a Bruker D8 advance powder diffractometer equipped with a Cu $K\alpha$ radiation source.

EMR spectra at *X*-band (9.45 GHz) were recorded by using a Bruker Elexsys E500 spectrometer equipped with a continuous-flow ^{4}He cryostat (ESR 900, Oxford Instruments) to work at variable temperature. Angular-dependent spectra were recorded by rotating the tube by means of an automated goniometer (ER218PG1, Bruker). The EMR spectra were acquired using a field modulation of 100 kHz and 5 G, and a microwave power of 6.5 μW. Magnetic measurements were performed on water solutions using a QD MPMS SQUID magnetometer. Magnetic data were corrected for the diamagnetic contributions of the solvent and of the sample holder, which were measured separately.

III. PREPARATION OF LiDps AND FERRITIN PROTEINS CONTAINING MNPs

The addition of Fe(II) to the apo-LiDps and apo-PfFt proteins (450 or 4500 atoms/protein, respectively) was carried out as described in the Experimental section. Iron incorporation results in the formation of dark brown solutions containing $\geqslant$ 95% or 90%, respectively, of the initial proteins. Accordingly, there was little precipitate after centrifugation of the solutions at the end of the reaction, while bulk precipitation of iron hydroxide polymers occurs in control reactions run in the absence of proteins. The amount of iron in the major peaks isolated from size exclusion chromatography for the LiDps and PfFt samples was estimated to be 405 or 4050 atoms/protein, respectively, on the basis of ferrozine assay and quantitative protein assays,[22] an indication that most of the iron added forms the protein-enclosed oxide nanoparticles. Analytical ultracentrifugation (AUC) was used thereafter to assess the molecular mass and size distribution of the iron particles synthesized in the protein cavities. The particle size distribution was calculated with the program SEDFIT (provided by Dr. P. Schuck, National Institutes of Health) by taking into account the densities of the proteins (1.35 g/cm^3) and of bulk maghemite (4.9 g/cm^3) and the thickness (2 nm) of the protein shell.[27] The size distributions of the MNP-containing LiDps or PfFt solutions thus calculated have their maximum at 3.4 and 7.7 nm and a standard deviation of 1.0 and 1.4 nm, respectively (Fig. 1).

The average size of the MNPs was confirmed by TEM images (Figs. S1 and S2 in the supplemental material[33]), which showed for both samples the presence of uniform spherical nanoparticles with average size $d = 3.2 \pm 0.8$ nm and 6.7 ± 1.5 nm for LiDps and PfFt, respectively. The XRD pattern of PfFt MNPs (Fig. S2 in the supplementary material[33]) exhibited diffraction peaks that were indexed as (220), (311), (511), and (440) reflections, characteristics of the cubic spinel structure of magnetite and maghemite, or any intermediate composition, which could not be discriminated owing to significant line broadening due to the small size of the crystalline domains. The broadness of the peaks of LiDps particles prevented the phase

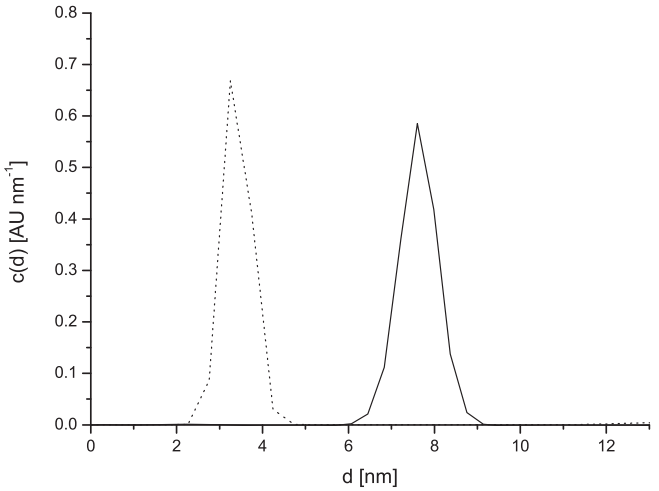

FIG. 1. Size distributions of the MNPs in LiDps (dashed line) and PfFt (continuous line) solutions obtained by AUC.

identification by XRD. However, previous high-resolution TEM analysis demonstrated that the adopted synthetic procedure provides particles with lattice spacing matching the one expected for maghemite/magnetite.[22] In addition, a control has been performed by the magnetic characterization, leading to the same conclusions.

IV. MAGNETIC MEASUREMENTS

Hysteresis loops of frozen solutions of PfFt and LiDps were recorded at 1.8 K and the results are shown in Fig. 2. The saturation magnetization values, M_S, estimated by fitting the high-field data to the empirical law $M = M_S + a/H + b/H^2$, were $M_S = 71.4$ emu g^{-1} Fe_2O_3 for PfFt and 59.7 emu g^{-1} for LiDps. The remnant magnetizations, $M_R = M_{0T}/M_{5T}$, were 0.44 for PfFt and 0.27 for LiDps, and the coercive fields, B_C, 305 and 335 G, respectively. The M_S values are lower than the corresponding bulk one (∼80–90 emu/g for magnetite, 70–80 emu/g for maghemite) as expected for nanometric particles. Anyway they fit among the largest value commonly observed,[34] pointing out the high crystallinity of

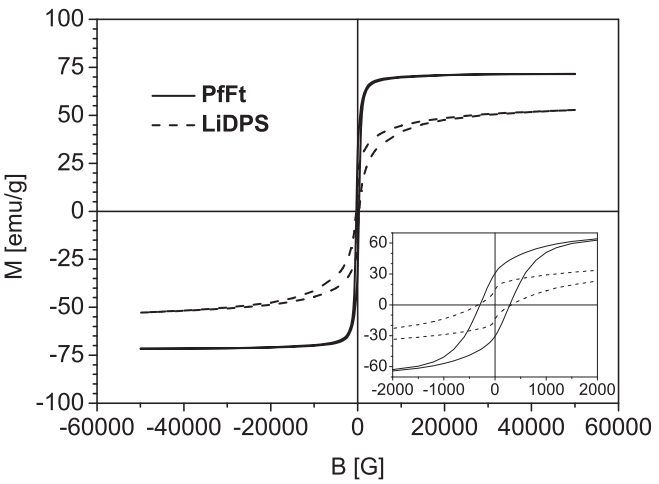

FIG. 2. Hysteresis loops recorded at 1.8 K. The low-field behavior is evidenced in the inset.

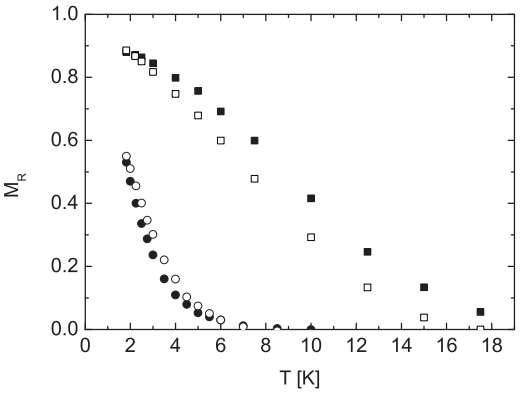

FIG. 3. Reduced remnant magnetization, M_R, directly evaluated from the hysteresis loops measured as a function of the temperature (open symbols) and from the fraction of unblocked MNPs, $x(T)$, as described in the main text (full symbols) for LiDps (circles) and PfFt (squares).

the material. The hysteresis loop of LiDps shows a butterfly shape due to the presence of a fast relaxing component which produces a sharp decrease of the magnetization around zero field. Indeed, due to the small average size, a relevant part of LiDps nanoparticles is in the superparamagnetic regime even at 1.8 K. Due to the larger size of the particles such behavior is not observed in the PfFt sample. Accordingly, M_R is close to 0.5 for PfFt (corresponding to randomly oriented particles with uniaxial anisotropy all in the blocked state) while it is much lower for LiDps. Measurement of the hysteresis loops at variable temperature indicated that, as expected, M_R decreases for both samples on increasing temperature, approaching 0 for 7.0 K (LiDps) and 17.5 K (PfFt), see Fig. 3. For both samples a remarkable high field irreversibility is observed, which is a typical signature of the presence of a disordered spin layer,[35] as indeed often observed for very small MNPs.[22,34] Accordingly, the smaller nanoparticles exhibit a larger irreversibility field (∼25 and 17 kG for LiDps and PfFt, respectively).

The zero-field-cooled (ZFC) and field-cooled (FC) magnetization curves of the samples, recorded from 2 to 220 K

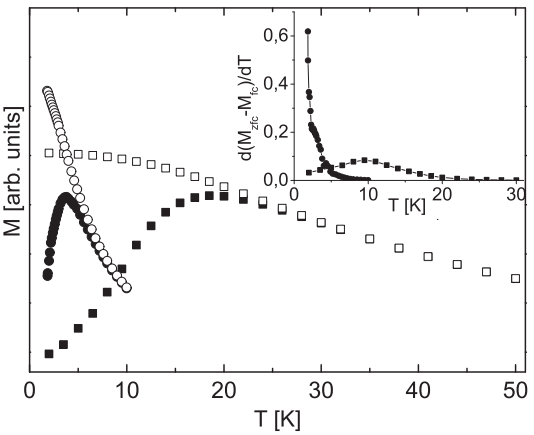

FIG. 4. ZFC (full symbols) and FC (open symbols) magnetization curves for PfFt (squares) and LiDps (circles). The inset shows the normalized blocking temperature distributions.

TABLE I. Comparison of the magnetic parameters of iron oxide MNPs precipitated in LiDps and Ferritin (Ft) proteins presented in this work and in Gilmore *et al.*[41] and Li *et al.*[29]

	Size (nm)	KV/k_B (K)	τ_0 (s)	B_a (kG)		
				$2K/M_S$	B_c vs T	EMR
LiDps	3.4[a]	65.6	1.0×10^{-10}	3.02	~3	/
PfFt	7.7[a]	539	1.6×10^{-13}	1.79	1.4	0.476
LiDps	4.9,[b] 3.5[c]	190,[b] 71.7[c]				2.4[b]
HsFt	8,[b] 7[c]	318,[b] 448[c]				0.9[b]

[a]Estimated from sedimentation velocity profiles as these data are representative of the whole sample.
[b]Reference 29.
[c]Reference 41.

by applying a 50 Oe probe field, are shown in Fig. 4. The average blocking temperatures, T_B, taken as the maxima of the ZFC curves, are 18.5 K for PfFt and 4 K for LiDps. The irreversibility temperature is very close to T_B (28 K for PfFt and 6.5 K for LiDps), indicating that the size distribution is quite narrow, confirming that a good size control has been achieved.

A quantitative evaluation of the energy barrier distribution can be obtained by plotting the temperature derivative of the opposite of the thermoremnant magnetization defined as $M_{FC}-M_{ZFC}$ versus the temperature (inset of Fig. 4).[36] The data confirm the qualitative indications provided by the analysis of the field dependence of M. Indeed, the integral of the normalized curve up to the temperature T gives the fraction of unblocked MNPs as a function of temperature, $x(T)$. The latter is directly related to the reduced remnant magnetization by[37] $M_R = 0.5*[1-x(T)]$.

While for PfFt, in the investigated temperature range, the progressive unblocking of all the MNPs was observed, for the smaller particles mineralized in LiDps the blocking-unblocking process can be monitored only for the high size portion of the distribution. It is worthwhile to underline the nice agreement, evidenced by the plots of Fig. 3, between the values of M_R obtained by the two independent magnetization measurements, namely the ZFC/FC and the hysteresis curves at variable temperature.

An evaluation of the anisotropy field $B_a = 2K/M_S$, where K is the anisotropy energy constant, can be obtained from the temperature dependence of the coercive field,[38]

$$B_C(T) = 0.48B_a(1 - \sqrt{T/T_B}). \quad (1)$$

Equation (1) holds only for particles in the blocked state, that is, for $T \ll T_B$, which is not the case of the experiments performed in this work. Thus the measured B_C must be corrected by subtracting from the hysteresis loop the contribution to the magnetization arising from the superparamagnetic component, which reduces the coercive field values.[37,39] The calculation, the details of which are described in the supplementary material,[33] yielded $B_a = 1.4$ kG for PfFt and ~3.0 kG for LiDps. The difference between the two samples reflects the higher anisotropy, which, due to the larger contribution of the surface, characterizes smaller MNPs.[40] We also note that the LiDps value is larger than that previously reported in Ceci *et al.* ($B_a = 1.4$ kG), where B_a was evaluated neglecting the role of the fast relaxing component.

The anisotropy fields can also be directly evaluated by definition once M_S and K are known ($B_a = 2K/M_S$). The values for the former have been obtained from the low-temperature hysteresis loops, while the latter can be obtained from the investigation of the dynamics of magnetization reversal by measuring the temperature dependence of the ac susceptibility at different frequencies (1–1000 Hz) between 1.8 and 150 K (Fig. S4 in the supplementary material[33]). Following the same analysis reported by Ceci *et al.*,[22] anisotropy energy barriers (KV/k_B) of 539(7) and 65.6(1.9) K were obtained for PfFt and LiDps, respectively, and values of the attempt time, τ_0, of the order of 10^{-13}–10^{-10} s (see Tab. I). The τ_0 values are in the expected range for independently relaxing superparamagnetic systems and indicate that dipolar interactions are negligible. On the basis of the values obtained for the energy barriers and considering the average diameter of the particles extracted from sedimentation velocity study, the anisotropy constants K for the two systems can be estimated as 4.40×10^5 erg/cm^3 for LiDps and 3.11×10^5 erg/cm^3 for PfFt. These are in agreement with the values reported by Gilmore *et al.* for particles of similar size,[41] and provide B_a values of 3.02 kG (LiDps) and 1.79 kG (PfFt), which confirm the estimation obtained by the analysis of the temperature dependence of B_C.

The magnetic parameters obtained for the two compounds by the different experimental methods are summarized in Table I and compared to the corresponding quantities reported in the literature.

V. TEMPERATURE DEPENDENCE OF X-BAND EMR SPECTRA OF MNPs IN PfFt AND LiDps

The temperature dependence of the EMR spectra acquired at X-band of PfFt and LiDps is shown in Fig. 5. For PfFt, the spectra are dominated by a composite signal centered approximately at $B_0 = 3400$ G. In particular, in the range 250–150 K, two signals are clearly observed, a broad one and a sharp one. As the temperature decreases, both become broader: the linewidth of the sharp component varies from 198 to 354 G and that of the broad component from 732 to 1097 G on varying the temperature from 250 to 150 K. The widening of the broad line depends on the anisotropy field of the MNPs, which becomes more effective, as the temperature is decreased, in influencing the resonance position of the MNPs. A fitting procedure, using a linear combination of two first-derivative Gaussian curves, was used to obtain a reliable estimate of the two contributions in the whole temperature range.

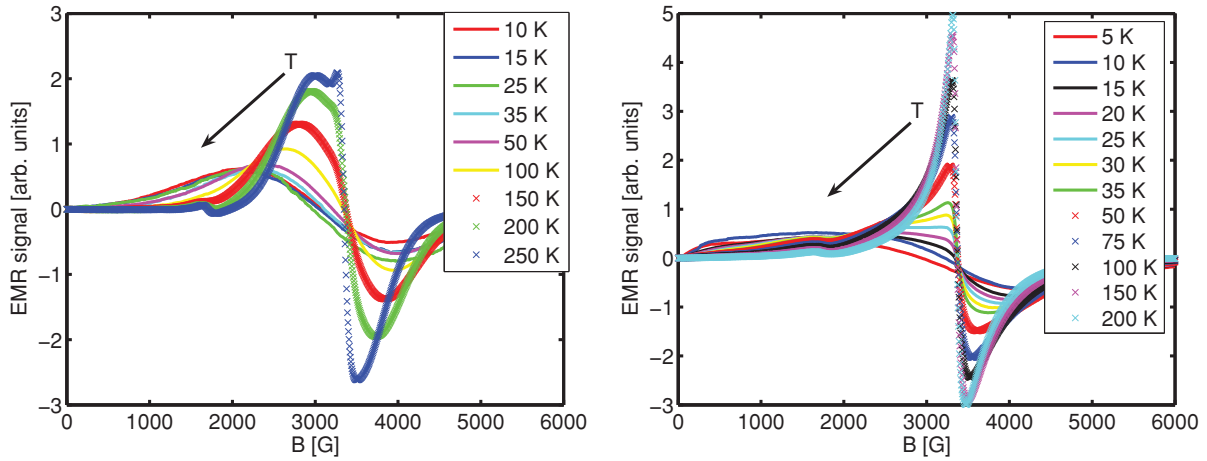

FIG. 5. (Color online) *X*-band EMR spectra of PfFt (left) and LiDps (right) suspensions frozen in zero field acquired at various temperatures.

A similar behavior is observed for LiDps: however, the presence of the sharp signal is less evident in this case, since the broad line is narrower than the corresponding one of the PfFt, which has a larger energy barrier than that of LiDps.

In addition to the main resonance, a band at field values corresponding to $B_0/2$ (g value $= 3.57$ at 200 K for PfFt, B_0 signal occurring at $g = 1.932$) is observed for both samples. This is quite well resolved for PfFt in the temperature range 250–150 K, while it can be observed down to approximately 50 K in LiDps. It occurs at a g value clearly different from the $g = 4.3$ of the well-known Fe^{3+} paramagnetic species and with a temperature behavior different from that of a paramagnetic system.[22] This signal has been attributed to formally forbidden $\Delta M = \pm 2$ transitions, which may be observed in small MNPs.[23] To the best of our knowledge, this is reported for the first time for MNPs mineralized in the PfFt shell, while it was observed by some of us in LiDps.[22] The clear observation of such transitions in the EMR spectrum points out the discreteness of the energy levels also in the MNPs, which are the subject of this study. The width of the half-field signals parallels that of the corresponding high-field signal and is therefore broader at a given temperature for PfFt than for LiDps.

VI. ORIENTATION DEPENDENCE OF EMR SPECTRA

EMR spectra of PfFt suspensions frozen (200 K) in the presence of a magnetic field ($B_f = 6000$ G) have been acquired with the aim of characterizing the properties of the portion of MNPs that have their anisotropy axes aligned with $\mathbf{B_f}$. After freezing, the sample tube was rotated around its own axis to acquire EMR spectra with the static magnetic field forming an angle θ with the direction defined by $\mathbf{B_f}$ in the sample. The EMR spectra recorded at $\theta = 0°$ and 90° are shown in Fig. 6. The major spectral feature is centered at $\sim g = 2$ ($g = 1.932$ at 200 K) and shows at least two signals. However, a quantitative deconvolution requires to consider three components: a sharp one (signal A), a broad one with no orientation dependence (signal B), and one that shows orientation dependence (signal C). We assign signal B to the fraction of randomly oriented MNPs, and C to those particles that had their easy axes aligned along $\mathbf{B_f}$. Finally, signal A must be attributed to particles for which the broadening features are minimized. This occurs for the fraction of randomly oriented particles that are oriented with the easy axis making an angle close to 54.74° (magic angle) with the magnetic field. We will comment on this point in the following, focusing for the moment on signals C and B. It is worth noting that the separation of MNPs in two subensembles, an oriented and a nonoriented one, is somehow rough, since there is actually a continuous variation between these two behaviors, which can even be recognized in the EMR spectra. However, this simple schematization gives a good physical insight into the problem, and we will retain it. In Fig. 7, the deconvolution obtained by simulation of the central line ($g \sim 2$) with three Gaussian derivatives is shown for EMR spectra acquired at $\theta = 0°$ and 90°. This allowed us to estimate the difference between the resonance fields (B_r) of signal C at $\theta = 0°$ and 90° as $\Delta = B_r(90°) - B_r(0°) = 600$ G. This is approximately three times larger than that observed by Li *et al.* in the field frozen spectra acquired at 77 K on 8.0 nm MNPs in horse spleen ferritin.[29] We attribute this

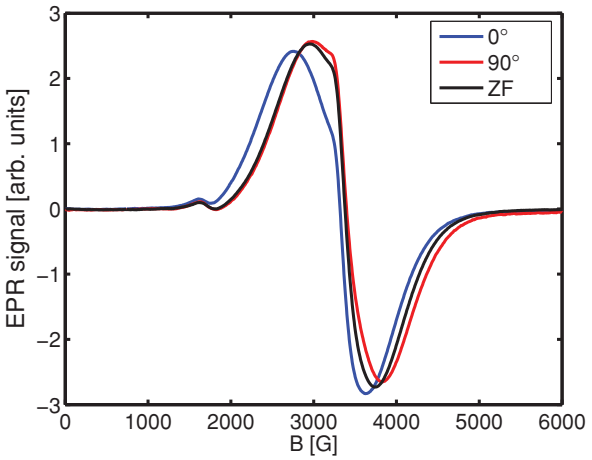

FIG. 6. (Color online) EMR spectra of PfFt frozen in field and acquired at $\theta = 0°$ (blue line) and $\theta = 90°$ (red line) and of the suspension frozen in zero field (black line).

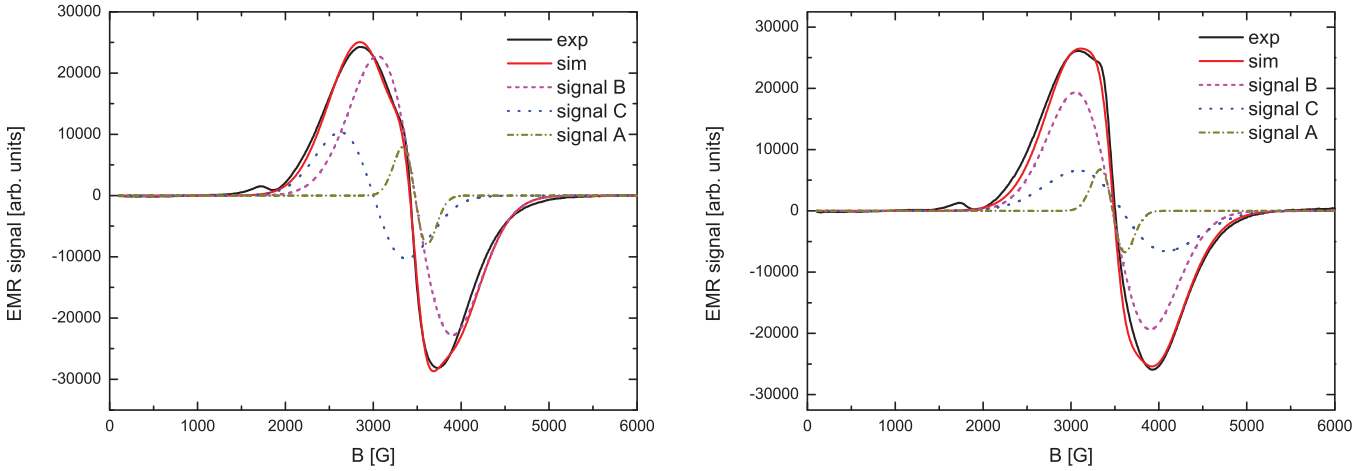

FIG. 7. (Color online) Deconvolution of the *X*-band EMR spectra of field frozen PfFt acquired at $\theta = 0^\circ$ (left panel) and $\theta = 90^\circ$ (right panel). Black: experimental spectrum; red: simulation; magenta: simulation of signal B; green: simulation of signal A; blue: simulation of signal C.

discrepancy to the different analysis performed by Li *et al.*, who have measured the resonance fields on the whole broad signal without distinction between signals *C* and *B*.

The orientation dependence of the resonance field predicted by a classical model,[20,21] in the strong field approximation ($B_0 \gg B_a$), and uniaxial anisotropy is given by the relation

$$B_r = \frac{\omega_0}{\gamma} - \frac{B_a}{2}\frac{L_2}{L_1}(3\cos^2\theta - 1) \qquad (2)$$

where $L_2(x) = 1-3\ L_1(x)/x$, $L_1(x) = \coth(x) - 1/x$ is the Langevin function, and $x = M_S VB/k_BT = \mu B/k_BT$, and θ is the angle between the external field and the easy axis of the considered MNP. The assumption of uniaxial anisotropy is supported by the reduced remnant magnetizations and by the full orientation dependence of the EMR spectra (see also Fig. S5 in the supplementary material[33]), in which only one maximum and one minimum appear and a $\cos^2\theta$ dependence of the resonance field is observed. The value $B_a \frac{L_2(x)}{L_1(x)}$ is referred to as B_a^{eff}. From the experimental difference Δ, the anisotropy field, B_a, can be determined:

$$\Delta = \tfrac{3}{2} B_a^{\text{eff}} \qquad (3)$$

Using the M_s value obtained by the magnetic measurements, $B_a = 0.48$ kG is derived. This value is significantly lower than that obtained from the magnetic characterization. Possibly the difference arises from the fact that we are dealing here with the subensemble of MNPs which more easily orient their easy axes along $\mathbf{B_f}$, that is, MNPs with larger magnetic moment, that is, larger dimension and lower anisotropy field. For a similar reason, the value of B_a which we estimated from the EMR data is almost half of that obtained by Li *et al.*,[29] which, as for the magnetic measurements, is an average value over the MNP size distribution. For this subensemble, the *g* value of 1.986 can be obtained from Eq. (2).

It is interesting to note that for signal *C*, the linewidth (ΔB) is larger at 90° than at 0° (see Table II). An opposite trend is reported by Li *et al.*[29] This discrepancy is due to the fact that here we are characterizing an oriented subensemble, without the broadening induced by a distribution of easy-axis orientations. Therefore, in the case presented here the results provide the intrinsic orientation dependence of the linewidth.

Contrary to PfFt, the suspension of LiDps frozen in field did not show any orientation dependence of the EMR spectra. This may be ascribed to the fact that the MNPs in LiDps are smaller than in PfFt. A similar behavior has been reported in 2–3 nm magnetite nanoparticles.[42]

Beyond the major feature at B_0 discussed so far, a signal at approximately $B_0/2$ is also present in the EMR spectra of the ferritin sample frozen in field. Compared with the main signal, this shows a weaker orientation dependence, which could, however, be clearly evidenced by simulations (see Fig. 8). These were performed at each orientation considering two contributions, both Gaussian derivatives, in analogy to signals *B* and *C* of the main feature. The first one well reproduces (except for the intensity) the $B_0/2$ signal in powder spectra and the second one accounts for the θ dependence. The difference in the experimental resonance fields, $\Delta_{B/2} = B_{r,B/2}(90^\circ) - B_{r,B/2}(0^\circ)$, is 55 G, approximately ten times smaller than that

TABLE II. Resonance fields, B_r, and linewidths, ΔB, of the three signals obtained from the deconvolution of the EMR spectra of PfFt for the zero-field frozen suspension and for the suspension frozen in field ($B_f = 6$ kG) at $\theta = 0^\circ$ and 90° with respect to $\mathbf{B_f}$.

	Signal	B_r (G)	ΔB (G)
$\mathbf{B_f} = 0$	A	3474	280
	B	3474	904
$\theta = 0^\circ$	A	3474	280
	B	3474	850
	C	2980	830
$\theta = 90^\circ$	A	3474	280
	B	3474	850–950[a]
	C	3580	1000

[a]The value 850 G fits better for the high-field part of the spectrum, while 950 G better reproduces the low-field part.

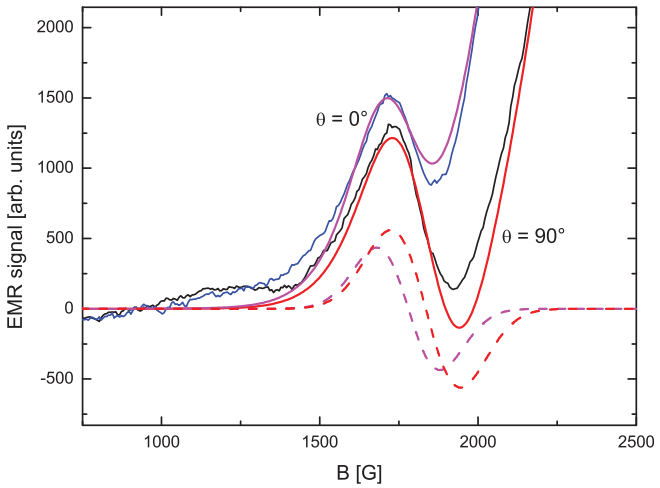

FIG. 8. (Color online) Deconvolution of the *X*-band EMR spectra of PfFt acquired at $\theta = 90^\circ$ and 0° in correspondence of the $B_0/2$ transitions. Simulation includes two Gaussians for each orientation: an orientation-independent contribution and a second one that is orientation-dependent. The latter is indicated by the dashed line for the two orientations.

observed for the main resonance. Finally, we note that bands at $B_0/3$ are also observed for PfFt (see Fig. 8).

The origin of these low-field transitions can be rationalized by considering the results reported for EMR spectra of lower-dimensional magnets. The presence of satellite lines $2\omega_0$ and $3\omega_0$ is brought about by dipolar perturbation. In three-dimensional (3D) magnetic systems, for which the condition of fast exchange regime holds, these lines are effectively pushed under the envelope of the main line. However, in lower-dimensional magnets, this regime does not hold and satellite lines may be observed.[43] In a first approximation, the surface of the MNPs can be regarded as a 2D magnetic lattice with respect to the exchange interaction, instead of the 3D one of the subsurface ions. On decreasing the MNP size, this 2D magnetic lattice will play an increasingly pronounced role. Moreover, it has been shown that on decreasing the dimension, the surface disorder propagates in MNP for a relevant part.[34,35] This is in line with the fact that the half-field transition was reported up to now only for very small MNPs.[22–24] We wish to stress here that, since the ac susceptibility measurements demonstrated that each MNP is magnetically isolated, the perturbation that induces the half-field transition is an intraparticle interaction (given by surface anisotropy and magnetocrystalline anisotropy and not an interparticle one (dipolar)).

VII. DISCUSSION IN THE QUANTUM FRAMEWORK

The rich EMR behavior of the measured MNPs give us the chance to understand the role and the order of magnitude of the different energy terms: exchange, anisotropy, and Zeeman. In this framework, signals *A* and $B_0/2$ will be discussed using a model based on a quantum-mechanics approach that, similarly to molecular clusters, associates a giant spin *S* to each particle. The giant spin is determined by the exchange interaction. The spin Hamiltonian used to describe the MNP EMR spectra, expressed in the reference frame with the axis *z* directed along $\boldsymbol{B}$ and making an angle θ with the anisotropy axis $\boldsymbol{n}$, can be written as[44]

$$\frac{\hat{H}}{\hbar} = \gamma B \hat{S}_z + \frac{D}{2}\left\{(3\cos^2\theta - 1)\left[\hat{S}_z^2 - \frac{S(S+1)}{3}\right] + \sin\theta\cos\theta[\hat{S}_z(\hat{S}_+ + \hat{S}_-) + (\hat{S}_+ + \hat{S}_-)\hat{S}_z] + \frac{\sin^2\theta}{2}(\hat{S}_+^2 + \hat{S}_-^2)\right\} \quad (4)$$

Assuming axial anisotropy, the *D* parameter is related to the classic anisotropy field by $B_a = -2SD'$, where $D' = D/(g_e\mu_B)$.[12] In zeroth-order approximation, the energy levels are determined by the first two terms of Eq. (4) and the corresponding states are eigenstates of the $\hat{S}_z$ operator. The microwave field, $\boldsymbol{B}_1$ perpendicular to *z*, induces the allowed transitions with $\Delta M = \pm 1$. In the strong field approximation ($B_0 \gg B_a$), the resonance fields for the $M \rightarrow M+1$ transitions are given by the relation

$$B_r = (3\cos^2\theta - 1)(D'/2)(1 + 2M) + B_0, \quad (5)$$

where *M* are the eigenvalues of the $\hat{S}_z$ operator. In a ferromagnetically coupled cluster the resolved fine structure, associated with Eq. (5), collapses on increasing *S* due to the decrease of *D*.[12] This is particularly true at the so called magic angle ($3\cos^2\theta - 1 = 0$, where the contribution of the second-order anisotropy field (ZFS) cancels and all the transitions collapse to B_0 ($g = 2$) independently of *M*.

The sharp line observed in MNP spectra, particularly evident at high temperatures, had been previously attributed to the thermal population of levels with low $|M|$ in conjunction with the presence of *D* strain.[25] Indeed, according to Eq. (5), transitions from low $|M|$ levels occur at resonance fields closer to B_0 and are less broadened by *D* strain. However, even in the absence of *D* strain, the same effect would be observed due to the coalescence of all transitions in correspondence with the magic angle. Indeed, the same sharp component can be simulated also with the classical model,[12] in which the resonance field, given by Eq. (2), has the same orientation dependence of Eq. (5). Another possible interpretation, which will be discussed later on, attributes the appearance of the sharp line to the magnetic decoupling between the surface and the core in the MNPs.[42]

The observation of the sharp peak *A* in the spectra of Figs. 6 and 7 corresponding to $\theta = 90^\circ$ and 0° is therefore a sign of the incomplete orientation of the MNP easy axes along the $\mathbf{B_f}$ direction.

More comments are needed for the half-field transitions, which acquire intensity through admixing of the adjacent states $M \pm 1$ due to the nondiagonal matrix elements of the operators $\hat{S}_z\hat{S}_\pm$ in the third term of Eq. (4). The intensity of the transitions, $M \rightarrow M+2$, has been calculated by Noginova *et al.*,[23]

$$\frac{I_{B_{0/2}}}{I_{B_0}} = 8\sin^2\theta\cos^2\theta\left(\frac{B_a}{B_0}\right)^2\left[\frac{x - 3L(x)}{x^2 L(x_0)}\right] \quad (6)$$

where $x = M_S V B_0/2k_B T$, $x_0 = 2x$. The intensity of the transitions at $B_0/2$, $I_{B_{0/2}}$, is zero at the extremes, $\theta = 0^\circ$ and 90°. It should be noted that a similar result would be obtained by including dipole-dipole interaction between particles, which are, however, excluded in our case.[23] Therefore,

the fact that the half-field feature is observed in EMR spectra of the field-cooled PfFt sample also at the extremes confirms that only a partial alignment of the particle easy axes occurs on freezing in the field.

In particular, since Eq. (6) shows that $I_{B_{0/2}}$ is zero at $\theta = 0^\circ$ and 90° while the contributions at these orientations are different from zero for the related allowed transitions at B_0, the fraction of orientations that give a nonzero contribution in the half-field transition can be estimated from the ratio $2\delta_{B0/2}/\delta_{B0}$, resulting in 0.44. Here δ_{B0} and $\delta_{B0/2}$ are the widths observed in the powder spectrum, determined by $\Delta B_{\rm eff}$ and $\Delta B_{\rm eff}/2$, respectively, being $\vec{\rm B}_{\rm eff} = \vec{\rm B}_0 + \vec{\rm B}_{\rm a}^{\rm eff}$. The variation in the resonance field observed at $B_0/2$ (55 G) can be compared with the value estimated by the relation

$$\Delta_{\rm B_0/2} = \frac{2\Delta_{\rm B_0}\delta_{\rm B_0/2}{\rm L_1(B_0)L_2(B_0/2)}}{2\delta_{\rm B_0}{\rm L_2(B_0)L_1(B_0/2)}} \tag{7}$$

which predicts a value of $\Delta_{B0/2} \sim 90$ G. The comparison with the experimental value is reasonably good given the fact that in Eq. (7) we do not take into account that the variation comes from a partially ordered contribution. Indeed, strictly speaking, the subensemble that gives the orientation dependence of $B_0/2$ is different from that giving the orientation dependence around B_0. Furthermore, a non-negligible error affects the experimental value, which is difficult to extract due to the partial overlap with the main resonance. However, the reasonable agreement obtained shows that this transition is a forbidden transition related to the main feature at B_0.

At *W*-band (95 GHz and 33 kG for $g = 2$), the band at $B_0/2$ could not be observed for PfFt; it was observed instead for LiDps, although with very low intensity (see Fig. S6 in the supplemental material[33]). From Eq. (6), the field dependence of this band at very large B_0 can be estimated:

$$\frac{\rm I_{B_{0/2}}}{\rm I_{B_0}} \propto \frac{\rm B_a^2 k_B T}{\rm B_0^3 M_s V} \tag{8}$$

Equation (8) predicts that the intensity of this band decreases as B_0 increases and it is smaller for MNPs with smaller anisotropy field and larger magnetic moment, which is the case for PfFt in comparison to LiDps.

It is interesting to point out that, on the basis of the previous discussion, both signal *A* and the $B_0/2$ one derive from MNPs that have approximately the same orientation with respect to the direction of $\mathbf{B_f}$. Indeed, the first one derives from particles with θ close to the magic angle, 54.74°, while the latter reaches the maximum intensity for $\theta = 45^\circ$. A similar behavior is observed in the *W*-band EMR spectra of an iron-based molecular nanomagnet, namely, the Fe_{19} oxyhydroxide cluster.[31] The single-crystal EMR data on this system confirm the prediction of Eq. (6), the $B_0/2$ feature being absent for field orientation parallel and perpendicular to the easy axis and reaching a maximum around θ values of 45°–55°. A wealth of EMR data together with a blend of experimental and theoretical approaches allowed us to obtain a deep insight into the electronic structure of the Fe_{19} cluster. The iron (III) ions in Fe_{19} are coupled to give a spin ground state $S = 35/2$ with a close-lying first excited state $S = 33/2$.

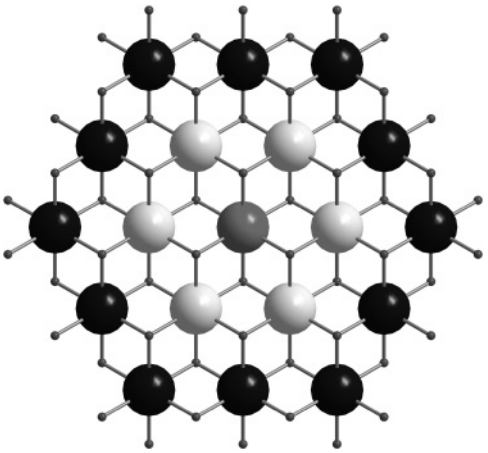

FIG. 9. Scheme of the growth of brucite-type clusters. Sphere of different colors corresponding to different generations. The red spheres represent oxygen atoms.

The estimated energy separation between the two states is around 8 K. The *D* parameter of the ground state was found to be -0.03 cm^{-1}, corresponding to an anisotropy field of approximately 10 kG, with a ratio $B_a/B_0 \sim 0.3$ very close to the value for PfFt and LiDps MNPs investigated at 9 GHz. The similarity of this ratio makes the comparison with MNPs particularly suited since it determines the relative importance of the different terms in the Hamiltonian [Eq. (4)] and therefore the intensity of the different features in the EMR spectra. However, the relative complexity of the structure of this cluster and its low symmetry makes it difficult to obtain a complete picture of the low-lying energy level pattern and its effect on the EMR spectra. Indeed, Fe_{19} has a structure close to that of brucite,[45] with the lattice that grows following the scheme sketched in Fig. 9. The first generation has one metal ion, the second $1+6$, the third $1+6+12$, and so on, with the outer ring at the *N*th generation having $6N$ ions. For clusters following this growth scheme, the ions of the outer ring can be considered as surface, in analogy to the core-shell separation in MNPs. However, while Fe_{19} has large deviations in the outer ring of the second generation, an almost ideal brucite structure is present in the Mn_{19} cluster,[32] which follows the brucite growth rule up to the third generation. Its magnetic and EMR properties are appealing because manganese (II) is a d^5 ion with $S = 5/2$ like iron (III). In particular, from the width of the EMR spectra data, the estimation of the anisotropy, $2DS$, of $\sim$10 kOe can be obtained.[46] This is most probably an underestimation. Nevertheless, this last value may explain [Eq. (8)] the observation of a quite intense $B_0/2$ feature in the EMR powder spectra recorded at *W*-band.[46]

The ideal structure of Mn_{19} makes it also a good model to understand the structuring of the energy levels: indeed, its symmetry is such that three coupling constants are needed to describe the magnetic coupling in the $10^{14} \times 10^{14}$ Hilbert space of 19 spins $S = 5/2$. Antiferromagnetic coupling is dominant with associated spin frustration effects in the triangular lattice. The Monte Carlo approach fitted the experimental susceptibility well with $J_1 = 24$ K, $J_2 = 16$ K, and $J_3 = 3$ K. The detailed scheme of the *J* coupling is reported by Lima *et al.*[46] (see also Fig. S7 in the supplemental material[33]).

According to this approach, the coupling constants of the internal core Mn_7 are much larger than those involving the external Mn_{12} ring. It is possible, therefore, to start from a simplified model in which the Mn_7 core is treated with the *HDvV* spin Hamiltonian and the Mn_{12} ring is assumed to be noninteracting. For the Mn_7 centered ring, it is also possible to give analytical formulas for the energy levels; by using for the outer Mn_6 ring the approximation valid for big spins, the Hamiltonian can be written as

$$H = J_{AB}\mathbf{S_A} \cdot \mathbf{S_B} + J_1\mathbf{S_1} \cdot \mathbf{S_r}, \tag{9}$$

where $S_A = S_2 + S_4 + S_6$, $S_B = S_3 + S_5 + S_7$, $S_r = S_A + S_B$, $J_{AB} = (4/n)\ J_2$, with $n = 6$. By substitution of the J values obtained by Monte Carlo-based fit of the whole cluster, the ground state turns out to be $S = 5/2$, with excited states with $S = 7/2, 3/2, 9/2$ within 20 K.

The presence of the excited states lying close to the ground state in both the Fe_{19} and Mn_{19} clusters shows that a model based only on the S spin ground state is inadequate to describe the EMR spectra of these systems. This is even more relevant for MNPs, since on increasing the size of the nanomagnet the excited states will be closer in energy to the ground state. On the other hand, on decreasing the size of MNPs the role of the exchange interaction is weakened, producing a similar effect. Weak interactions are observed in Mn_{19} between the "core spin" and the "surface spin," which can model the MNPs behavior. Since the coupling J_3 is quite small compared to the other couplings, it is reasonable to assume that at high temperature, core and surface spins will be effectively independent of each other. This may well give rise to different signals in the EMR spectra of MNPs acquired at high temperatures.[41]

As a final remark, we also wish to point out that the spread in the shape of EMR spectra observed in the MNPs is not only determined by the anisotropy field but also by the energy anisotropy $|B_a\mu|$, which affects the values of L_1 and L_2 functions. So, even if smaller MNPs have larger B_a, mainly due to an enhanced surface anisotropy contribution, they have a smaller magnetic moment. This is again similar to the case of molecular nanomagnets, where the magnetic anisotropic barrier is given by $|DS^2|$ ($|D(S^2 - 1/4)|$ for half-integer spins).

In our case, the magnetic anisotropy energy is bigger for PfFt than for LiDps, as is apparent from both the magnetic data and the comparison of the total width of the EMR spectra of the two samples recorded at the same temperature. We may then expect that on further increasing the size, the surface anisotropy contribution will become negligible: the EMR central feature will become sharper and the $B_0/2$ and $B_0/3$ satellite lines (signature of the relevant role of the magnetic anisotropy) will disappear. This regime seems to be reached for maghemite MNPs already for dimensions of 19 nm[29] and clearly holds in bulk materials.

In conclusion, the magnetic properties of iron oxide MNP of different sizes mineralized within LiDps and PfFt protein cages were deeply investigated by magnetometric and EMR techniques. The estimation of the anisotropy fields was obtained by ac susceptibility measurements and from the temperature dependence of the hysteresis loop, and the results were compared to those evaluated by the analysis of the EMR spectra. The EMR behavior has been analyzed as a function of the temperature, of the microwave frequency, and of the orientation dependence of the field-frozen suspensions, and it has been compared with that of MNMs. This allowed us to assign the features present in the EMR of MNPs synthesized in ferritins. The sharp signal observed at $g = 2$ in the EMR spectra derives from MNPs with approximately the same orientation at which the $B_0/2$ signal appears. The last, therefore, belongs to the MNP main signal and it may be considered a fingerprint of the discreteness of the energy levels and of the quantum behavior of these systems. The analysis reported by Noginova *et al.*[23,24] had the merit to frame the study of MNPs in a quantum approach similar to that used for MNMs by associating a giant spin S to each particle. The study we presented here started from the same approach and tried to deepen this similarity by using the most recent findings on the EMR of MNMs. The results indicate that, in parallel to what occurs for MNMs, most of the temperature behavior of EMR spectra of MNPs has to be attributed to the contribution of excited (S) states and not only to the population of M levels lying at higher energies, as reported by Noginova *et al.*[23,24] These excited states are lying very close in energy to the ground spin state, as it is found experimentally for Fe_{19} and as it can be easily predicted for Mn_{19}. More generally, in MNMs, the energy gap between the first excited and the ground state is expected to decrease as the number of magnetic ions is increased.[12] Notwithstanding these limitations, we believe that the model based on the giant spin model offers a clear and elegant comprehension of the different and complex behavior of MNPs.

ACKNOWLEDGMENTS

E. Chiancone is gratefully acknowledged for continuous support in the realization of the work presented. César de Julián Fernández is acknowledged for fruitful scientific discussions. M.F. is grateful to MiUR and Ente CRF. C.I. and C.S. are grateful to EU for financial support through NANOTHER (FP7-NMP4-LA-2008-213631).

*maria.fittipaldi@unifi.it

†claudio.sangregorio@unifi.it

[1] A. H. Lu, E. L. Salabas, and F. Schuth, Angew. Chem., Int. Ed. **46**, 1222 (2007).

[2] A. H. Lu, W. Schmidt, N. Matoussevitch, H. Bonnemann, B. Spliethoff, B. Tesche, E. Bill, W. Kiefer, and F. Schuth, Angew. Chem., Int. Ed. **43**, 4303 (2004).

[3] T. Hyeon, Chem. Commun. (2003), 927.

[4] *Nanomagnetism and Spintronics*, edited by T. Shinjo (Elsevier, Amsterdam, 2009).

[5] S. Laurent, D. Forge, M. Port, A. Roch, C. Robic, L. V. Elst, and R. N. Muller, Chem. Rev. **108**, 2064 (2008).

[6] *Magnetism in Medicine: A Handbook*, edited by W. Andrä and H. Nowak (Wiley-VCH, Weinheim Germany, 2007).

[7]S. Chikazumi, S. Taketomi, M. Ukita, M. Mizukami, H. Miyajima, M. Setogawa, and Y. Kurihara, J. Magn. Magn. Mater. **65**, 245 (1987).
[8]A. K. Gupta and M. Gupta, Biomaterials **26**, 3995 (2005).
[9]Q. A. Pankhurst, J. Connolly, S. K. Jones, and J. Dobson, J. Phys. D **36**, R167 (2003).
[10]D. W. Elliott and W. X. Zhang, Environ. Sci. Technol. **35**, 4922 (2001).
[11]M. Takafuji, S. Ide, H. Ihara, and Z. H. Xu, Chem. Mater. **16**, 1977 (2004).
[12]M. Fittipaldi, L. Sorace, A. L. Barra, C. Sangregorio, R. Sessoli, and D. Gatteschi, PhysChemChemPhys **11**, 6555 (2009).
[13]W. Wernsdorfer, Adv. Chem. Phys. **118**, 99 (2001).
[14]J. Park, E. Lee, N. M. Hwang, M. S. Kang, S. C. Kim, Y. Hwang, J. G. Park, H. J. Noh, J. Y. Kini, J. H. Park, and T. Hyeon, Angew. Chem., Int. Ed. **44**, 2872 (2005).
[15]A. L. Barra, L. C. Brunel, D. Gatteschi, L. Pardi, and R. Sessoli, Acc. Chem. Res. **31**, 460 (1998).
[16]D. Gatteschi, A. L. Barra, A. Caneschi, A. Cornia, R. Sessoli, and L. Sorace, Coord. Chem. Rev. **250**, 1514 (2006).
[17]E. J. L. McInnes, *Spectroscopy of Single-molecule Magnets*, edited by R. E. P. Winpenny (Springer, Berlin, 2006).
[18]R. S. Edwards, S. Maccagnano, E. C. Yang, S. Hill, W. Wernsdorfer, D. Hendrickson, and G. Christou, J. Appl. Phys. **93**, 7807 (2003).
[19]S. Hill, S. Maccagnano, K. Park, R. M. Achey, J. M. North, and N. S. Dalal, Phys. Rev. B **65**, 224410 (2002).
[20]Y. L. Raikher and V. I. Stepanov, Zh. Eksp. Teor. Fiz. **102**, 1409 (1992).
[21]E. de Biasi, C. A. Ramos, and R. D. Zysler, J. Magn. Magn. Mater. **262**, 235 (2003).
[22]P. Ceci, E. Chiancone, O. Kasyutich, G. Bellapadrona, L. Castelli, M. Fittipaldi, D. Gatteschi, C. Innocenti, and C. Sangregorio, Chem. Eur. J. **16**, 709 (2010).
[23]N. Noginova, T. Weaver, E. P. Giannelis, A. B. Bourlinos, V. A. Atsarkin, and V. V. Demidov, Phys. Rev. B **77**, 014403 (2008).
[24]M. M. Noginov, N. Noginova, O. Amponsah, R. Bah, R. Rakhimov, and V. A. Atsarkin, J. Magn. Magn. Mater. **320**, 2228 (2008).
[25]N. Noginova, F. Chen, T. Weaver, E. P. Giannelis, A. B. Bourlinos, and V. A. Atsarkin, J. Phys. Condens. Matter **19**, 246208 (2007).
[26]E. Chiancone, P. Ceci, A. Ilari, F. Ribacchi, and S. Stefanini, Biometals **17**, 197 (2004).
[27]O. Kasyutich, A. Ilari, A. Fiorillo, D. Tatchev, A. Hoell, and P. Ceci, J. Am. Chem. Soc. **132**, 3621 (2010).
[28]M. Uchida, M. T. Klem, M. Allen, P. Suci, M. Flenniken, E. Gillitzer, Z. Varpness, L. O. Liepold, M. Young, and T. Douglas, Adv. Mater. **19**, 1025 (2007).
[29]H. Li, M. T. Klem, K. B. Sebby, D. J. Singel, M. Young, T. Douglas, and Y. U. Idzerda, J. Magn. Magn. Mater. **321**, 175 (2009).
[30]J. C. Goodwin, R. Sessoli, D. Gatteschi, W. Wernsdorfer, A. K. Powell, and S. L. Heath, J. Chem. Soc. Dalton Trans. 1835 (2000).
[31]L. Castelli, M. Fittipaldi, A. K. Powell, D. Gatteschi, and L. Sorace (unpublished).
[32]I. A. M. Pohl, L. G. Westin, and M. Kritikos, Chem. Eur. J. **7**, 3438 (2001).
[33]See supplemental material at [http://link.aps.org/supplemental/10.1103/PhysRevB.83.104409] for TEM and XRD data, and details of magnetic and EMR data analysis.
[34]A. Millan, A. Urtizberea, N. J. O. Silva, F. Palacio, V. S. Amaral, E. Snoeck, and V. Serin, J. Magn. Magn. Mater. **312**, L5 (2007).
[35]R. H. Kodama and A. E. Berkowitz, Phys. Rev. B **59**, 6321 (1999).
[36]J. L. Dormann, D. Fiorani, and E. Tronc, Adv. Chem. Phys. **98**, 283 (1997).
[37]P. Vavassori, E. Angeli, D. Bisero, F. Spizzo, and F. Ronconi, Appl. Phys. Lett. **79**, 2225 (2001).
[38]E. C. Stoner and E. P. Wohlfarth, Philos. Trans. R. Soc. London, Ser. A **240**, 599 (1948).
[39]W. C. Nunes, W. S. D. Folly, J. P. Sinnecker, and M. A. Novak, Phys. Rev. B **70**, 014419 (2004).
[40]*Surface Effects in Magnetic Nanoparticles*, edited by D. Fiorani (Springer, New York, 2005).
[41]K. Gilmore, Y. U. Idzerda, M. T. Klem, M. Allen, T. Douglas, and M. Young, J. Appl. Phys. **97**, 10B301 (2005).
[42]J. M. Vargas, E. Lima, R. D. Zysler, J. G. S. Duque, E. de Biasi, and M. Knobel, Eur. Phys. J. B **64**, 211 (2008).
[43]A. Bencini and D. Gatteschi, *EPR of Exchange Coupled Systems* (Springer-Verlag, Berlin, 1990).
[44]A. Abragam and B. Bleaney, *Electron Paramagnetic Resonance of Transition Metal Ions*, Oxford, (1970).
[45]D. J. Price, F. Lionti, R. Ballou, P. T. Wood, and A. K. Powell, Philos. Trans. R. Soc. London, Ser. A **357**, 3099 (1999).
[46]N. Lima, A. Caneschi, D. Gatteschi, M. Kritikos, and L. G. Westin, Inorg. Chem. **45**, 2391 (2006).